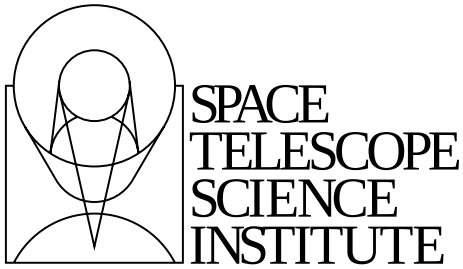

Instrument Science Report WFC3 2005-16

Scientific Impacts of UVIS Channel Filter Ghosts

Howard E. Bond & Thomas M. Brown

April 14, 2005

ABSTRACT

Several of the filters currently installed in WFC3 produce significant ghost artifacts, arising from reflections between optical surfaces within the filters. The ghosts are particularly severe in F225W, reaching as high as ∼15% of the source flux. Weaker ghosts are seen in F275W, F606W, and F656N. In all, a total of nearly two dozen filters have detectable ghosts. In all cases the structure of the ghosts changes significantly across the field of view, sometimes to a very large degree. The intensity of the ghosts also varies strongly with the spectral energy distribution of the target. At the request of the WFC3 SOC, we have carried out simulations of the impact of these ghosts on various kinds of scientific programs, and investigated several methods for mitigation of these effects.

For uncomplicated scenes covering a small spatial extent, such as host galaxies surrounding isolated QSOs, the effects of ghosts are fairly minimal, even with F225W. PSF deconvolution algorithms, such as Lucy-Richardson, can remove such ghosts quite well. However, once the scene covers a significant field of view, the strong dependence of ghost structure on field position means that no existing software can deconvolve the image. In such cases, if the field is not too complex, images taken at different dither positions and/or different spacecraft roll angles can be combined in such a way as to remove the ghosts to a considerable extent. However, for extended targets such as nebulae or galaxies, especially those with a wide dynamic range, the ghosts cause irretrievable loss of information, especially in faint portions of the objects adjacent to bright regions. This can be true even with filters having faint ghosts, such as F656N.

We also simulated the effects on crowded-field stellar photometry. The impact depends strongly on the nature of the stellar field (i.e., how crowded, how many bright stars), but in many cases, even in F225W, the effect on the derived color-magnitude diagrams is fairly modest. The effects can be reduced further by combining images taken with large dithers or changes in roll, but in general the slight improvement in the photometry will not be worth the loss in field or the additional observing time.

Because of the significant impact of ghosts as severe as those of F225W on some types of scientific programs, we recommend a more detailed cost-benefit analysis of replacement of this filter with one that is ghost-free. If any of the filters discussed here are flown, it will be necessary to provide a significant level of support to scientists who are preparing observing proposals for WFC3. This advice will have to be provided before Phase I, since it affects the amount of observing time that must be requested to carry out each program.

Introduction

It was discovered during testing of the WFC3 UVIS CCD channel in late 2003 and early 2004 that a subset of the 62 optical and UV filters produce significant ghosts, as described in detail by T.M. Brown & O. Lupie (April 2004, ISR WFC3 2004-004). Subsequent tests under ambient conditions (T.M. Brown & O. Lupie, July 2004, ISR WFC3 2004-012) and during thermal-vacuum testing (T.M. Brown, February 2005, ISR WFC3 2005-001) have confirmed that the ghosts have remained present, and are not significantly altered when the instrument is operated in vacuum.

The ghosts arise from several categories of reflections involving the filter surfaces, including those surrounding the air gaps in the filters, and between the CCDs and the dewar windows. These ghosts appear variously as donut-shaped rings or more complex shapes extending away from star-like sources, and/or a complex pattern of nearly point-like ghosts in the vicinity of bright sources.

The appearance of the ghosts is, in many cases, highly dependent on the location of the source within the field of view (FOV). In some cases, the ghost artifacts point roughly radially away from the center of the FOV. In others, the series of ghosts is nearly parallel across much of the FOV, all of them extending away to the upper left of the stellar source, for example. Still other ghosts, however, have locations relative to the illuminating source that vary only slightly with field location.

The ghost structures are dependent on the spectrum of the source (and depend even on light from well outside the main bandpass of the filter). See Brown and Lupie (ISR WFC3-2004-004) for data regarding the strong variation of the ghost intensity with source wavelength and hence the strong dependence of the integrated ghost intensity on the spectral energy distribution of the target.

The existence of these filter ghosts has raised considerable concern about their potential impacts on WFC3 science programs. An analysis of these impacts is the subject of this document.

The SOC Action Item

At its November 2004 meeting, the WFC3 Scientific Oversight Committee (SOC) issued an action item to the WFC3 Integrated Product Team (IPT) as follows:

> *[E]xplore observational strategies and software to mitigate effects of filter ghosts. Quantitatively examine sample science applications where ghosts are likely to have big effects. Examples are (i) host galaxies of QSOs; (ii) multiband photometry of globular star clusters; and (iii) photometry of the M31 bulge. What impact on science quality or observational efficiency will be produced by ghosts? Study consequences for observations in the following three filters: F225W, F275W, F606W.*
> (—R.W. O'Connell, January 2005, minutes of WFC3 SOC meeting 23.)

The three filters identified above by the SOC exemplify essentially the full range of ghost phenomena seen with the WFC3 filter complement. However, we decided to add one narrow-band filter which is likely to be widely used, the Hα filter F656N, to the list of those to be studied. Table 1 presents brief descriptions of the ghost features that accompany these filters.

Table 1
SELECTED UVIS FILTERS WITH SIGNIFICANT GHOSTS

Name	Remarks
F225W	Bright distorted donut ghosts, totalling ∼15-17% of source flux for red sources and 2-3% for UV-bright sources; extend away from source toward upper left for many field positions
F275W	Bright donut ring, totalling ∼0.7% of source; found on side of source radially away from center of field
F606W	Numerous point-like ∼0.1% ghosts with weak dependence on field location; large faint donuts on side away from field center
F656N	Small and large rings and donuts, totalling ∼0.5%; small rings generally lie above or to upper left of source

Fig. 1 shows examples of the ghosts in the F225W, F275W, and F606W filters. In all three cases, the calibration stimulus (CASTLE) has placed a point-like source in the upper right quadrant of the WFC3 FOV (namely, at either the "UV14" or "B" location described below). The FOV is 256×256 pixels, or $10\farcs0 \times 10\farcs0$ projected onto the sky.

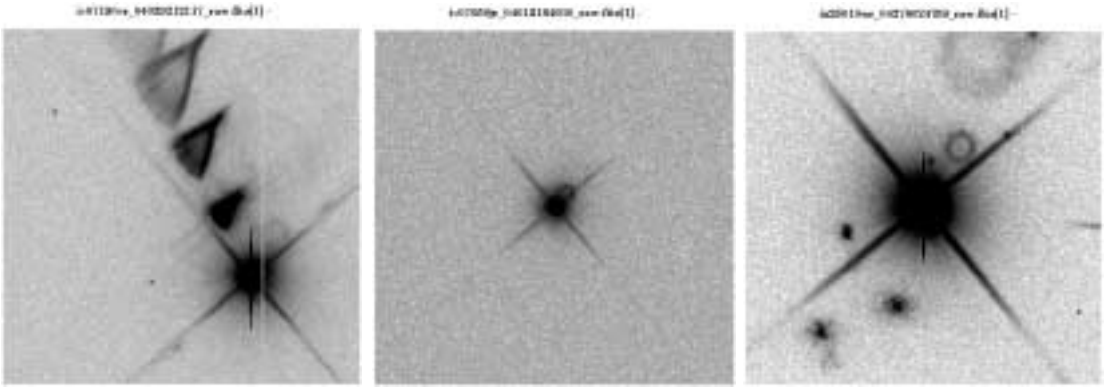

Figure 1: Examples of filter ghosts in long test exposures in (**left**) F225W, (**center**) F275W, and (**right**) F606W. In these exposures, an artificial star was placed in the upper right corner of the WFC3 field of view. The "star" is saturated, and a logarithmic stretch is used to display each image. Field of view is 256×256 pixels or $10\farcs0 \times 10\farcs0$. F225W shows a sequence of distorted ghosts extending to the upper left; F275W has a circular donut just to the upper right of the star; and F606W has several nearly point-like structures to the lower left of the star as well as a series of small and large donuts to the upper right. Ghosts in F656N (not shown) are similar to the bright ring to the upper right of the source in F606W.

Although the images in Fig. 1 appear to show very serious ghosting, we point out that the test exposures were for very bright artificial stars, and that a hard logarithmic stretch is used in the figures showing the ghosts in this document. These renditions thus strongly emphasize the impact of the ghosts, and there may well be some applications in which the effects of the ghosts on the science will be fairly minimal. This issue is explored in depth later in this document. Finally, in this connection, it is worth mentioning that *all HST* images contain one conspicuous set of artifacts, namely the diffraction spikes surrounding every stellar source. For example, in images taken with the F225W filter, the diffraction spikes contain approximately 1% of the source intensity. Astronomers are so accustomed to accepting these artifacts that they hardly even notice them.

Location-Dependent Behavior

The filters also show a variety of location-dependent behaviors. Fig. 2 illustrates the nomenclature adopted in this report for field locations referred to below. UV13, UV14, UV15, and UV16 were defined in an internal memo by G. Hartig (May 2003), and lie at the $(\pm 900, \pm 900)$ pixel coordinates. In subsequent test runs with CASTLE, the $(\pm 1600, \pm 1600)$ locations as well as $(0, \pm 200)$ were also used, and we have arbitrarily designated these points as "A" through "F," as shown in Fig. 2.

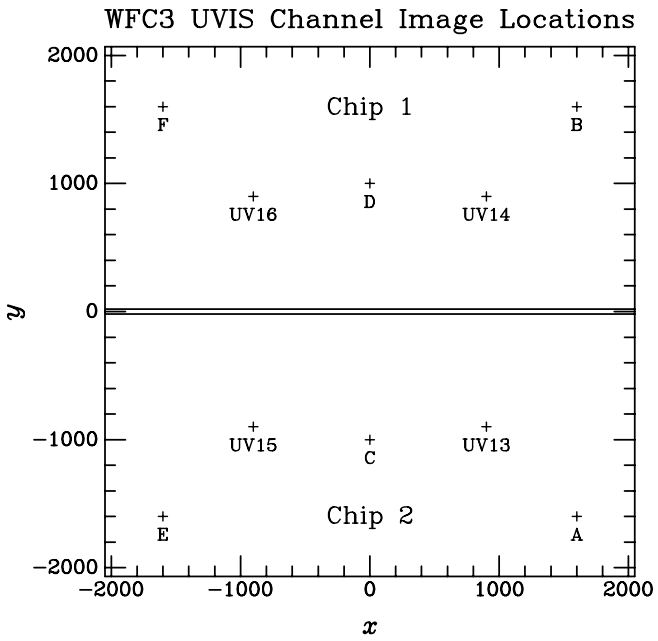

Figure 2: Nomenclature for image locations on the two WFC3 UVIS CCDs.

In Fig. 3 we show the ghost behavior for F225W, with the source placed at the four locations (UV13 through UV16) located about halfway from the center of the FOV toward the four corners. At these field positions, the ghosts lie in the direction to the upper left of the artificial star, i.e., they point radially away from a location lying around the lower right corner of the full FOV. However, further out from the field center there is a wider variety of angles.

Fig. 4 shows the contrasting behavior of the ghosts that affect F275W. These donut-shaped ghosts always lie on the side of the source facing away from the center of the FOV (suggesting that this filter may be mounted very close to perpendicular to the optical axis). The intensity of this ghost is considerably weaker than with F225W.

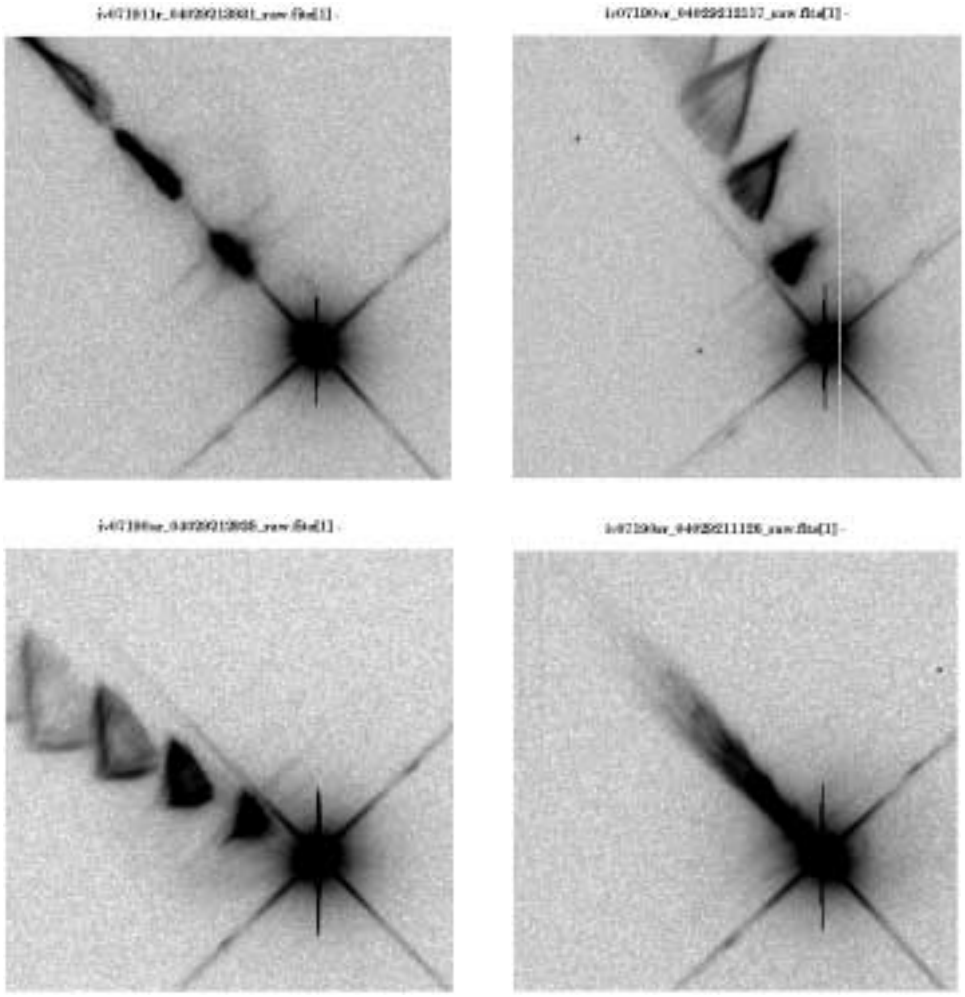

Figure 3: Filter ghosts in F225W, with the artificial star placed at the (**upper left**) UV16, (**upper right**) UV14, (**lower left**) UV15, and (**lower right**) UV13 field locations. Field sizes are 256×256 pixels or $10\farcs0 \times 10\farcs0$. These ghosts extend away from the source toward the upper left, with the angle varying slightly across the field. Further out from the field center, the angles vary more widely. Logarithmic stretch.

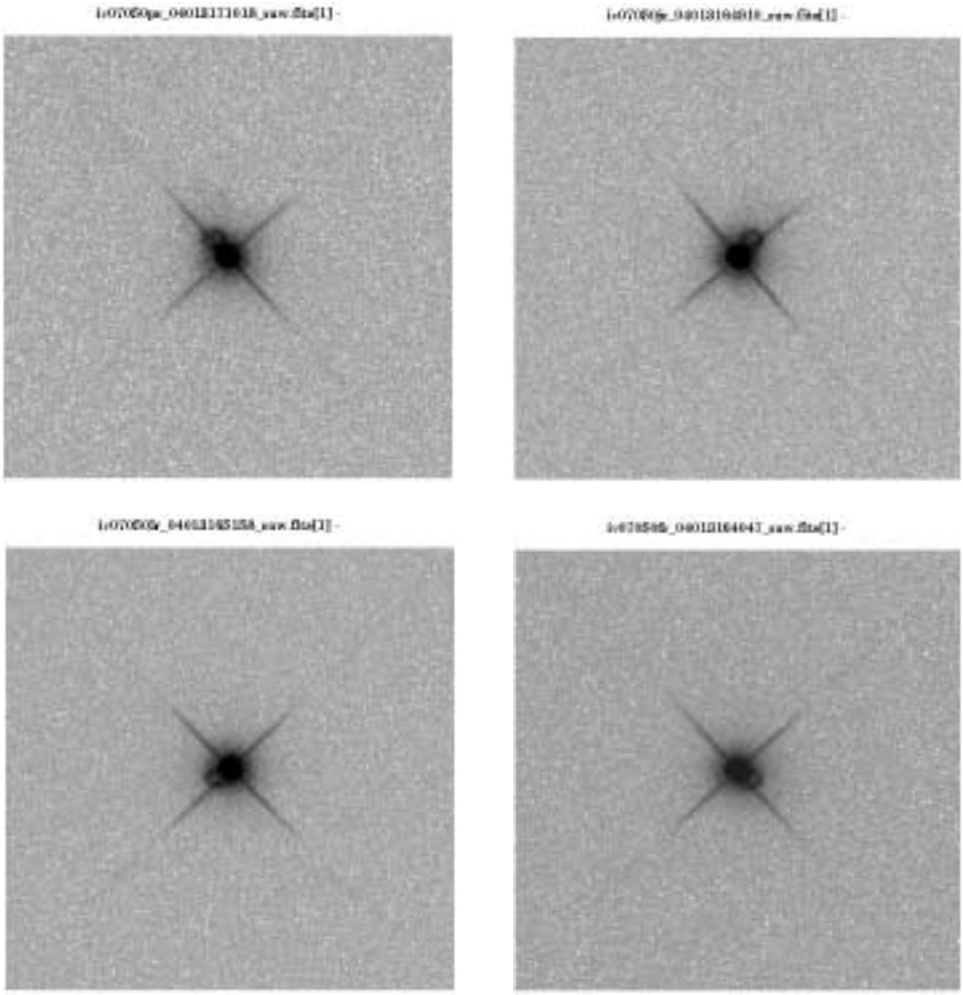

Figure 4: Filter ghosts in F275W, with the same field locations, field sizes, and logarithmic stretch as in Fig. 3. The ghosts in F275W appear as donuts lying about $0\farcs5$ from the source, always on the side of the source away from the center of the field of view.

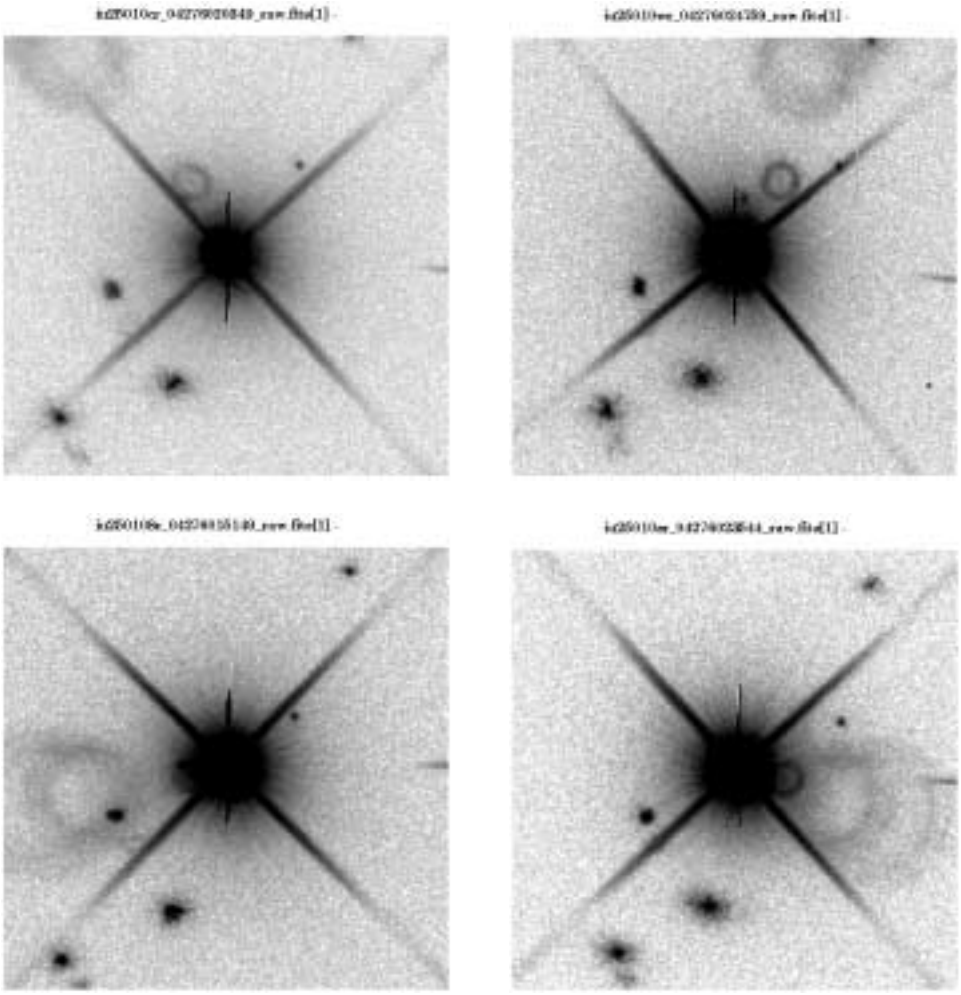

Figure 5: Filter ghosts in F606W, with the artificial star placed at the (**upper left**) F, (**upper right**) B, (**lower left**) E, and (**lower right**) A field locations. Field sizes are the same as in Fig. 3, and a log stretch is used. There are three kinds of ghosts in F606W: (1) compact, almost point-like ghosts lying mostly to the lower left and upper right of the source, with their locations relative to the source being nearly independent of field location; (2) a donut similar to that seen in F275W (Fig. 4), lying roughly on the side of the source away from the center of the FOV; and (3) larger and fainter donuts, also on the side away from the center. The ghosts in F656N (not shown) are similar to the small bright rings in the upper left and upper right images

Mitigation Strategies

We will now explore approaches toward mitigating the effects of the filter ghosts described above. We will consider four basic strategies, as summarized in Table 2. They are listed in order of increasing impact on observing time and usable field of view.

Table 2
GHOST MITIGATION STRATEGIES

Strategy	Description
Accept ghosts	Use ghost-affected data as is
PSF deconvolution	Use cleaning algorithms to remove ghosts
Dither mitigation	Place target at several positions in FOV
Roll mitigation	Use several different spacecraft roll angles

Impact of Ghosts on Direct Imaging of Extended Objects

As an initial example, we will consider the first scientific application mentioned by the WFC3 SOC in its action item, namely the study of QSO host galaxies. This is a case where, typically, there is a single bright star-like object in the FOV, surrounded by low-surface-brightness "fuzz." The science investigation generally involves morphological classification of the fuzz (spiral, elliptical, or interacting? star-forming or quiescent?), and perhaps simple quantitative measurements (e.g., the brightness profile of the host galaxy).

Accept Ghosts

In cases such as these, involving essentially visual descriptions of the morphology and simple quantitative measures in an uncrowded scene, the effects of the filter ghosts may well be minimal, and the images might be very useful "as is."

To simulate and explore the ghost impact, we extracted a WFPC2 image of a QSO and surrounding host from the archive. This image is of the QSO PG 0052+251 and was obtained by J. Bahcall in the F606W filter. There are 3 frames totalling 2100 sec, which we combined and cosmic-ray rejected. Since the core of the star-like QSO nucleus is saturated in all of the WFPC2 images, we artificially inserted a very bright pixel at its position. The image (taken in the WF3 chip) was next magnified by an amount that created a pixel scale equal to that of WFC3 ($0\farcs039$/pixel). We then convolved this image with a WFC3 PSF in the F225W filter from which we artificially removed the ghosts, in order to create a "truth" image. (Note that this procedure significantly degrades the resolution of the truth image relative to actual WFC3 performance because of the large pixels of the original WF3 image and the successive convolution with the WFPC2 PSF *and* again with the WFC3 PSF; however, we are interested here in the differential amount of additional degradation due to the filter ghosts.)

The "truth" image is shown at the upper left of Fig. 6. The QSO is clearly surrounded by a galaxy that can be classified morphologically as a spiral, and a number of structural details can be seen and simple measurements can be made. Next we convolve the image with the ghost-ridden PSF of F225W (instead of the ghost-free F225W used for the truth image), and the result is shown in the upper right of Fig. 6. Now a series of ghosts extending off to the upper left accompanies every bright object in the field, most obviously the very bright central QSO. It should be noted that this image exaggerates the ghost impact because the F225W PSF was determined using a very red source of illumination in the CASTLE; for a much bluer source such as the QSO, the ghosts will be fainter (for detailed measurements, see Table 3 of Brown & Lupie, 2004, ISR WFC3 2004-04). Also, of course, this simulation is not very astrophysically accurate, because an F606W image is being convolved with an F225W PSF.

Although almost all *HST* users would be unhappy with such a ghost-afflicted image, it is actually clear that the morphological classification of the host galaxy would be essentially unaffected in spite of the bright ghosts. However, quantitative measurements would certainly be compromised if no mitigations were employed.

The bottom left and bottom right panels in Fig. 6 show the images when convolved with the F275W and F606W PSFs. Due to the low relative intensities of the ghosts in these two filters, the images are insignificantly different, even for quantitative measurements, from the truth image. This is not surprising, since the S/N in the original image at typical locations $\sim 4''$ out from the nucleus in the spiral arms of the host galaxy is only about 15 per pixel. For the four ghost simulations shown in Fig. 6, the PSFs were taken at FOV locations UV14 (F225W, F275W) or B (F606W), as illustrated in Fig. 2.

PSF Deconvolution

Of course, because of ground- and space-based measurments, we will *know* the structure of the PSF, at least at certain pre-selected points in the FOV. The next level of complexity is to obtain an image of the target QSO at a fixed location within the FOV (such as UV14), and remove the ghost artifacts through PSF deconvolution, using the image of a bright isolated star at the UV14 location as the PSF. Sophisticated deconvolution algorithms were developed early in the *HST* program, following the discovery of the spherical aberration of the primary mirror.

To illustrate such a deconvolution, we applied the Lucy-Richardson algorithm (via the IRAF routine *lucy*). The resulting ghost-free image is shown on the left side in Fig. 7. Visually it is virtually indistinguishable from the truth image. To demonstrate this numerically, we calculated the difference between the Lucy-deconvolved image and the truth image, and the difference image is shown on the right in Fig. 7, with the image stretch enhanced by a factor of 10 relative to the image on the left. Apart from artifacts in the vicinity of bright objects, the differences are small (generally under $\sim 5\%$) compared to the S/N of the original image.

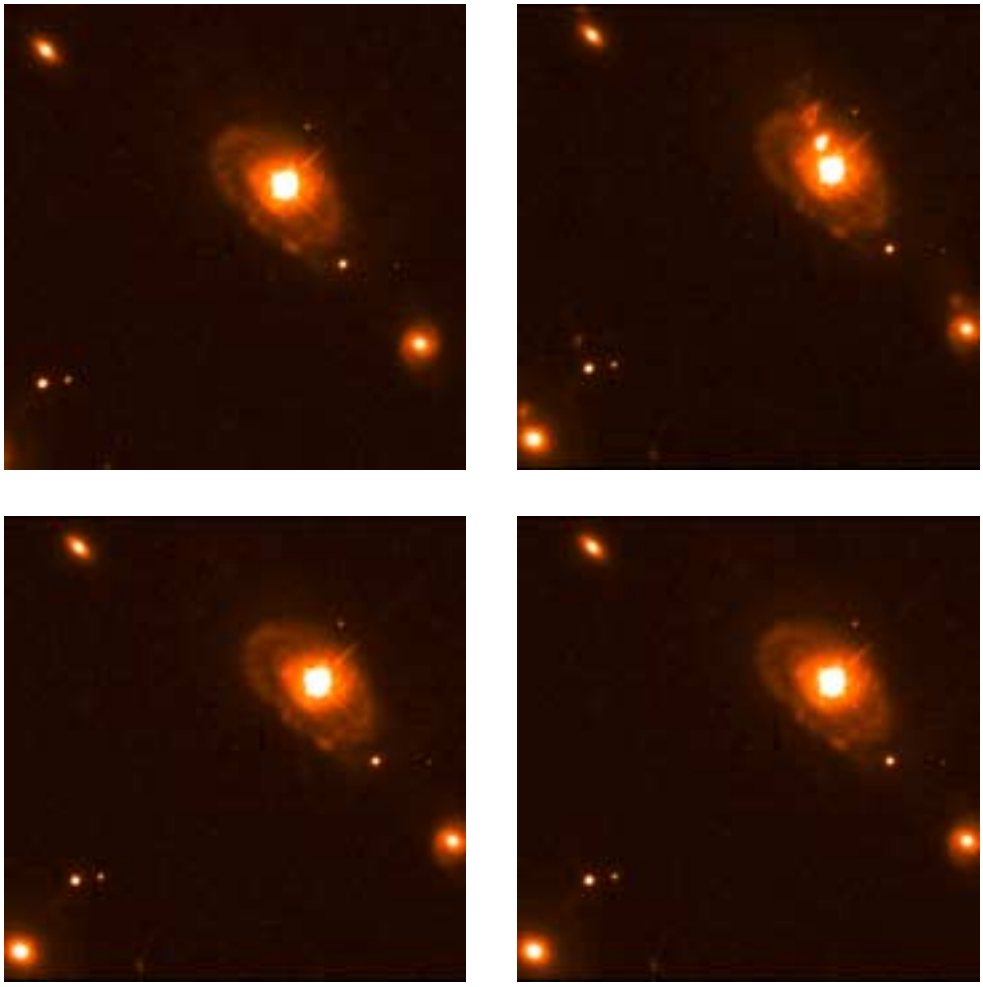

Figure 6: (**Upper left**) "Truth" image of QSO PG 0052+251 (WFPC2 image by J. Bahcall, convolved with ghost-free WFC3 F225W), showing the faint host spiral galaxy and several field objects; (**upper right**) image of PG 0052 convolved instead with the ghost-affected F225W filter. Note that bright ghost images of the luminous QSO in the nucleus have now appeared, but the morphology of the host galaxy is still easily classifiable. (**Lower left**) Truth image convolved with the F275W PSF; (**lower right**) truth image convolved with the F606W PSF. These two images differ negligibly, for all practical purposes, from the truth image, because of the low ghost intensities and modest S/N of the host galaxy image. Field of view is 800×800 pixels or $31'' \times 31''$, and the PSFs are for locations UV14 or B. Linear image stretches.

This simulation, of course, is not completely realistic, since the identical PSF was used both to create the ghost-affected image and then to deconvolve it. In practice, the *HST* PSFs at the times of the observations of the target and of the PSF reference star would have small differences due to telescope breathing and other time-dependent phenomena.

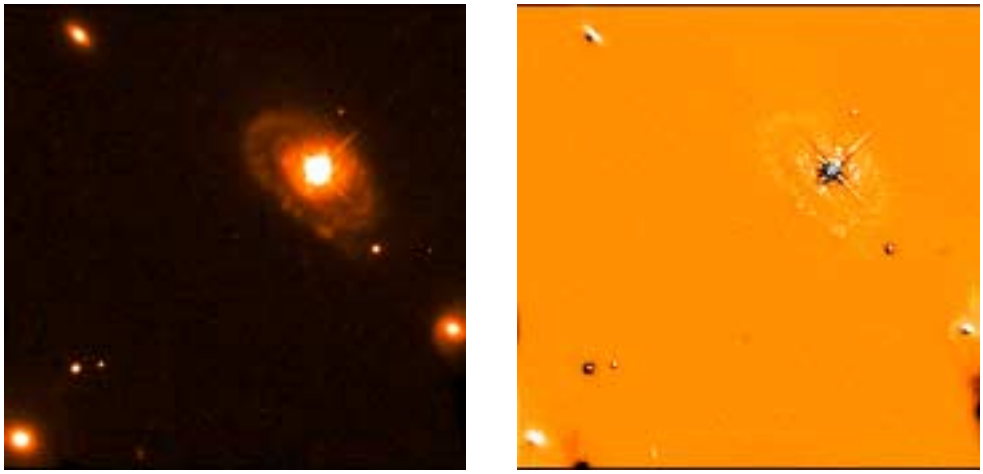

Figure 7: (**Left**) The ghost-affected F225W image of PG 0052+251 of Fig. 6 after deconvolution using the Lucy-Richardson algorithm; the ghost signatures have been removed almost completely. (**Right**) This image shows the difference between the deconvolved F225W image on the left and the truth image, with the image stretch enhanced by a factor of 10. Apart from artifacts near bright sources, the differences are small compared to the S/N. Linear stretches.

An even more serious problem, however, is that the F225W PSF varies rapidly across the field and with spectral energy distribution, whereas in our simulation we used an invariant PSF. Thus, the kind of deconvolution demonstrated here would really only be applicable over very small fields with little color variation and with adequate knowledge of the source energy distribution, and would be completely inadequate for the entire WFC3 FOV. To the best of our knowledge, deconvolution algorithms that can handle such a spatially rapidly varying PSF do not exist, and even if they did a very extensive series of measurements of the PSF at many points in the FOV would have to be available in order to apply such an algorithm.

Dither Mitigation

We now turn to a more complex scene than the QSO target. As an example, we will consider the planetary nebula (PN) NGC 6543 (also known as the Cat's Eye Nebula, a famous *HST* target). We downloaded from the archive an image of NGC 6543 taken with the ACS F502N ([O III]) filter by Z. Tsvetanov (GO-9026). Five bright artificial stars were inserted into the image, one at the center of the PN, and four around the corners of the image, to serve as tracers of the various convolutions. As was done above, we then convolved this image (this time neglecting the small difference in pixel scale between ACS [$0\farcs050$/pix] and WFC3 [$0\farcs039$/pix]) with a WFC3 F2256W PSF with ghosts removed, to create a "truth" image, shown at the upper left in Fig. 8. It is very difficult to render this image because of the enormous dynamic range, but we have chosen a logarithmic stretch that shows both some of the detail within the bright core of the PN, as well as

some of the remarkable features (periodic shells, rays pointing back to the central star) that *HST* has revealed in the faint halo.

The science to be done on an image like this would include descriptive discussions of the morphology, various geometric and intensity measurements of the features in the outer halo of the PN (such as the positions and surface brightnesses of the periodic shells, or the geometry of the rays pointing back toward the nucleus), and possibly measurements of the surface brightness of the PN in different filters.

We next convolved the ACS image with the F225W PSF to create the ghost-afflicted image shown at the upper right in Fig. 8. This image differs fundamentally from that of the QSO and host, which was a simple scene with mostly blank sky and only a few objects, dominated by a single bright point source. Now we have a very extended bright nebula covering most of the scene, with a large amount of ghost-induced "smearing" due to multiple overlapping ghosts of the extended nebulosity. There is no algorithm, even in principle, that can uniquely remove the PSF signature from an image like that at the upper right in Fig. 8. (We did go through the exercise of applying Lucy deconvolution. This resulted in an image that showed most of the qualitative features of the truth version, but with the surface brightnesses badly altered and incomplete removal of the ghosts around the bright stars even after 50 iterations.) The true situation is even worse, since the actual WFC3 PSF would vary continuously and quite considerably over a field of this large size, and as noted above we are not aware that algorithms exist that can handle deconvolution under such circumstances.

We can, however, try to take advantage of the PSF variation by using *"dither mitigation,"* by which we mean taking several images with the object placed at different locations in the FOV, and then combining them with a pixel-rejection algorithm. For an extended object like NGC 6543, it is evident that at least several dither positions will be required. (Consider, for example, a mitigation based on only two pointings, corresponding to the upper left and upper right PSFs in Fig. 3. It is clear that ghosts from adjacent bright nebulosities would intersect and thus could not be removed in any simple rejection algorithm.)

To test dither mitigation, we simulated images of NGC 6543 taken at the four positions defined in Fig. 3, i.e., UV13 through UV16, and then combined the 4 images using a CR-rejection algorithm and the noise characteristics of the camera. The result is shown in the lower-left image of Fig. 8. Although the bright, complex structures in the core of the PN are largely recovered, there are many low-level artifacts remaining in the faint halo. Some of these could potentially be misinterpreted as hydrodynamic features, when in fact they are not real.

A difference image between the dither-mitigated image and the truth image is shown at the lower right in Fig. 8. There is clearly excess flux at the upper left. This is not surprising, since the F225W ghosts all extend away to the upper left from a point source, albeit at angles that vary across the FOV. Thus, if we consider a pixel in the upper left quadrant of the faint halo, it receives spurious flux from the ghosts *in all four of the dither observations*, due to the bright extended region to the lower right. Hence, there is no way to recover the correct flux at this position through any rejection algorithm. The departures from the truth image, especially

at the upper left, are typically as high as 50–100% of the signal (due to light from the bright core spilling onto the much fainter halo).

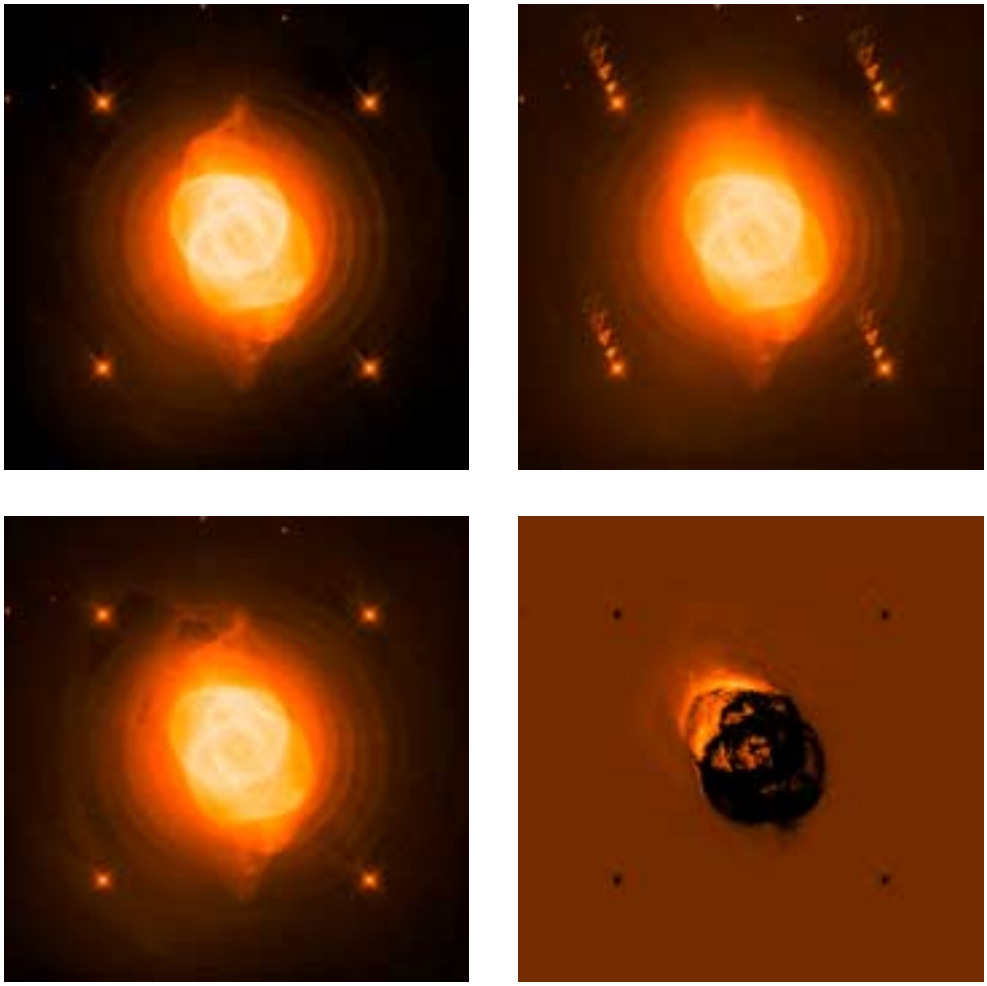

Figure 8: (**Upper left**) "Truth" image of planetary nebula NGC 6543 (ACS [O III] image by Z. Tsvetanov), convolved with ghost-free WFC3 F225W; (**upper right**) image of NGC 6543 convolved instead with the PSF of the WFC3 F225W filter at position UV14. Note the bright ghost images, especially of the artificially inserted stars near the four corners, along with considerable smearing of the nebula. (**Lower left**) Image mitigated by a 4-point dither. Structure of the bright portions of the nebula is largely recovered, but many low-level artifacts due to the ghosts remain in the faint halo around the PN. (**Lower right**) Difference image between the dither-mitigated image and the truth image. Excess flux and spurious artifacts are obvious at the upper left, along with low flux at the lower right. Field of view is 1400×1400 ACS pixels or $70'' \times 70''$. Logarithmic stretches for the first 3 images, linear for the difference image.

Our conclusion, for the F225W filter, is that dither mitigation can potentially recover some of the high-S/N features in a complex, extended, high-dynamic-range scene; but faint structures are badly compromised, especially when adjacent to brigher regions, even when four different dither positions are used.

We ran a similar simulation for the F275W filter, whose ghosts are much fainter and less complicated than those of F225W. In this case, we find that even an image taken at one dither position differs only insignificantly from the truth image, due to the low level of the ghosts.

Roll Mitigation

An alternative approach is what we call *"roll mitigation,"* in which images are taken at the same pointing but with various spacecraft roll angles, and then combined using rejection of bright pixels.

This method is expected to be promising for filters like F225W and F606W, where the ghosts tend to lie on the same side of the point source as we move around the FOV (see Figs. 3 and 5). Thus, at different spacecraft roll angles, the ghosts from a bright source will lie on different adjacent objects. However, roll mitigation will not work well with ghosts that are located at positions lying on the side of the point source radially away from the center of the FOV, such as the donut ghosts affecting F275W (see Fig. 4). This is because the ghosts from bright stars would always lie on the same faint stars, regardless of roll angle, and thus they cannot be removed with any simple sigma-rejection algorithm.

Moreover, roll mitigation using 90° rolls would require breaking up an observing program into widely separated scheduling windows, and would, for small programs, require a signficiant increase in the number of orbits required. (In some cases, it might be possible to use a smaller range of roll angles within a single scheduling window, at the cost of loss of area covered.)

We simulated roll mitigation of an F225W image by rotating the UV13 PSF by 90°, the UV15 by 180°, and the UV16 by -90°, and then convolving the NGC 6543 ACS image with each of the rotated PSFs (along with the unrotated UV14 PSF). Then we combined these four images, again using CR-rejection. The resulting image is shown on the left in Fig. 9. As compared with the dither-mitigated image in Fig. 8 (lower left), there are still fictitious artifacts in the faint halo of the PN, but at a considerably lower level. The right-hand image in Fig. 9 is the difference between the roll-mitigated image and the truth image, shown at the same stretch as in Fig. 8 (lower right). The difference image shows that the level of artifacts is quite a bit lower than with dither mitigation, mostly less than about 10% of the signal. This might be an acceptable level of ghost contamination for geometric measurements and morphological studies, but perhaps not for quantitative measurements of, for example, surface brightnesses in the faint halo.

The above simulations of the PN NGC 6543 were somewhat unrealistic, since it is unlikely that the F225W filter would be used in typical studies of planetary nebulae. However, expected uses of F225W, such as imaging large disk galaxies to map the ages of UV-bright star clusters, would exhibit analogous problems. The ghost strengths would be somewhat lower in intensity (the ghost intensities are lower for in-band UV light than for redder light) than modeled above; on the other hand, the variations in ghost intensity with local spectral energy distribution have not been taken into account in the discussion above.

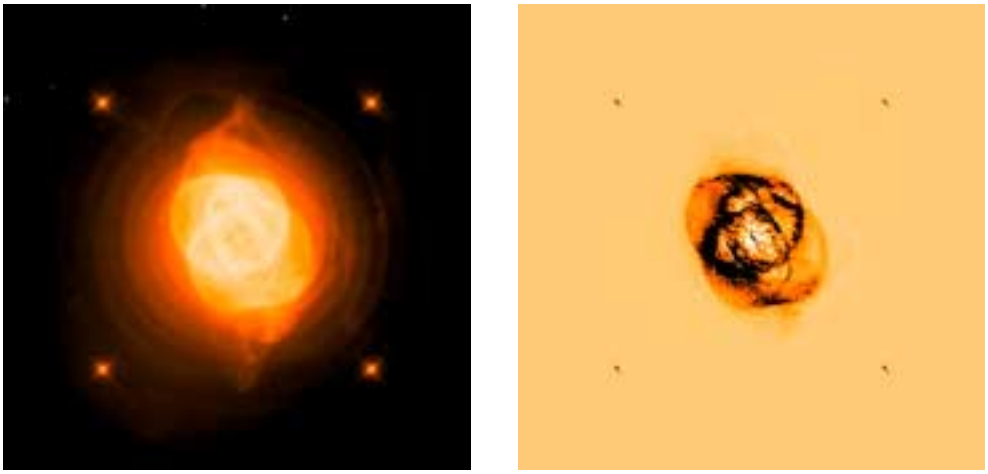

Figure 9: (**Left**) Image of NGC 6543 in F225W, corrected through a 4-angle roll mitigation. Low-level artifacts due to the ghosts remain in the faint halo, but are fainter than with the dither mitigation shown in Fig. 8. Same logarithmic stretch as in Fig. 8. (**Right**) Difference image between the roll-mitigated image and the truth image. Same linear stretch as in Fig. 8. Most surface-brightness discrepancies with the truth image are now below $\sim$10%.

Hα Imaging

A more common program for planetary nebulae would be observations in prominent emission lines. We therefore did another set of simulations using the narrow-band F656N filter that isolates the Hα emission line.

As described in Brown & Lupie (ISR WFC3 2004-004, 2004, Fig. 25), this filter has ring-shaped ghosts at about 0.5% of the source flux. Over most of the FOV, these rings tend to lie to the upper left of the source. Therefore, as in the case of F225W, we do not expect that simple dithering will be adequate to mitigate the ghosts.

As was done above, we first created a truth image of NGC 6543 by removing the ghosts from a F656N PSF image, and convolving it with the original ACS image. We then convolved the same original image with the PSF image with ghosts (at field position UV13), and the result is shown on the left side of Fig. 10. The ring-shaped ghosts are easily seen adjacent to bright stars, and would certainly compromise the image for, e.g., images intended for outreach purposes. Whether the image would be compromised for scientific purposes would, again, depend on the scientific goals; for general morphological studies or simple geometric measurements, this image might well be acceptable. However, departures from the truth image reach $\sim$30% of the signal in the portions of the faint PN halo just above the bright inner region, which would compromise surface-brightness measurements.

Combining images taken at different roll angles can mitigate ghosts of this type to a considerable extent. We simulated a combination of two images taken at rolls differing by 90°, with the rejection algorithm being a simple rejection of the brighter pixel at each point in the image. The result is shown on the right in Fig. 10. The rings adjacent to the bright artificial stars have now been effectively removed, and departures from the truth image within the nebula are generally below 10%. Use of additional roll positions would further improve the fidelity of the image.

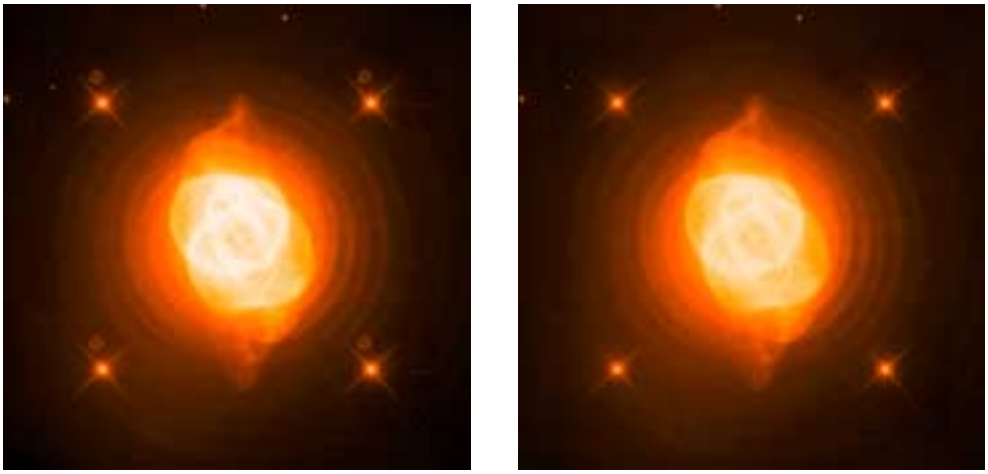

Figure 10: (**Left**) Simulated image of NGC 6543 in F656N, taken at a single pointing. Note faint ring-shaped ghosts to upper left of bright stars. (**Right**) Simulated F656N image after ghost removal by combining two images taken at roll angles differing by 90°. Same logarithmic stretches for both images. Spurious features in the faint PN halo are now generally well below 10% of the signal in the truth image.

Crowded-Field Photometry

We now turn to more quantitative types of measurements, which were also proposed in the SOC's action item, namely stellar photometry in crowded fields.

Intuitively, one might imagine that photometry of crowded star fields would suffer significantly from the ghosts in some of the UVIS filters. To investigate this, we simulated the data from two hypothetical globular-cluster programs, with one utilizing the F225W filter (which has the strongest extended ghosts) and the other utilizing the F606W filter (which has the strongest compact ghosts). In each program, we made the reasonable assumption that a color-magnitude diagram (CMD) would be created via pairing each of these filters with a filter that had no significant ghosts. For our simulations, the F336W was paired with the F225W, and the F438W was paired with the F606W.

F225W Simulations

For the F225W simulation, we created an artificial globular cluster (GC). A hypothetical population was created by combining the isochrones of Bertelli et al. (1994, A&AS, 106, 275) with the horizontal-branch (HB) evolutionary tracks of Brown et al. (2000, ApJ, 532, 308). The HB distribution was heavily skewed toward hot HB stars, because such a cluster might be a likely target for a UV stellar-populations imaging program that fully exploits the new capabilities of WFC3.

The assumed input population for the simulation is shown in Figs. 11 and 12, in which we plot physical (i.e., luminosities and effective temperatures) and observable (magnitudes and colors) parameters, respectively. The GC population was assumed to lie at a distance of 10 kpc, behind a small reddening of $E(B-V) = 0.02$, and spatially distributed in a Gaussian profile with $\sigma = 1100$ WFC3 pixels (i.e., $43''$), thus giving a range of crowding approximating what would be seen in an actual GC, even if the density profile is not completely realistic. The stars were randomly distributed in the HR diagram as appropriate for the relative lifetimes of the evolutionary phases shown. At each point in the HR diagram, the stellar parameters for a given star were used to interpolate in a grid of synthetic spectra (Castelli & Kurucz 2003, IAU Symp. 210, poster A20). The resulting stellar spectrum was then passed through the WFC3 throughput tool (Brown 2003, ISR WFC3-2003-13) to give predicted count rates in the F225W and F336W bands. Assuming exposure times of 5000 sec in each filter, these count rates were used to normalize a model of the WFC3 PSF, which was then added into each simulated image. The model PSF was calculated using TinyTim (Krist 1995, ASP Conf. Ser. 77, 349), assuming the ACS WFC PSF for the F435W filter, rotated by 45°; this is appropriate, given the better sampling of WFC3 but the shorter wavelengths (the decrease in the *HST* PSF width with decreasing wavelength levels off in the UV).

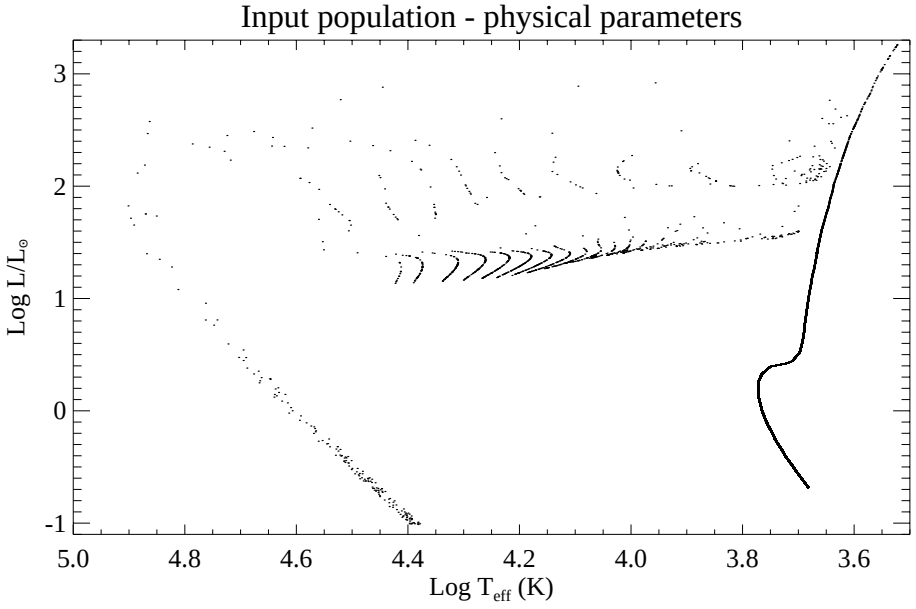

Figure 11: The input cluster population for the F225W and F336W simulated images, shown in terms of physical parameters for the 150,000 stars.

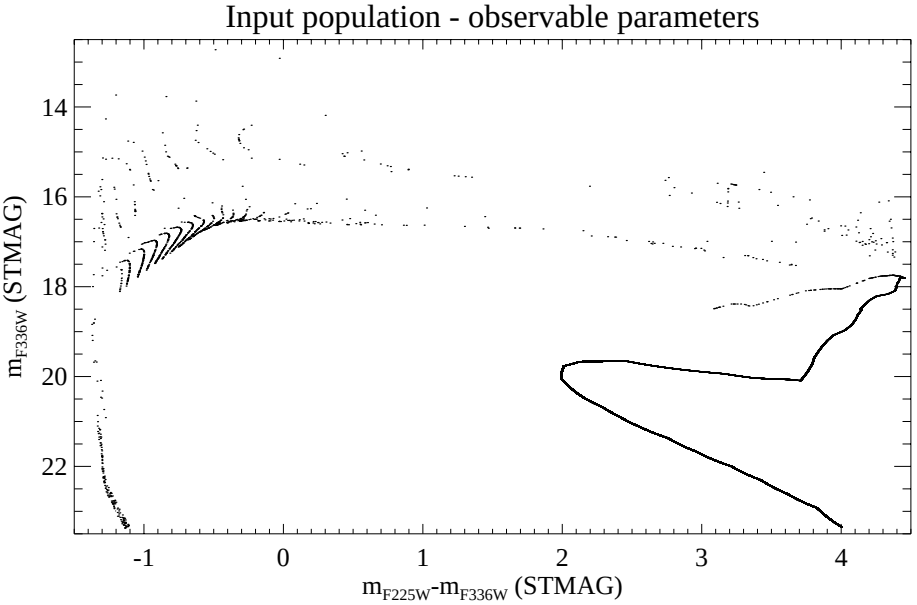

Figure 12: The input population for the F225W and F336W simulated images, shown in terms of observable parameters. The unusual appearance of the upper red giant branch is simply due to a lack of data in the transmission curve of the F336W filter at long wavelengths.

This process was iterated to produce 150,000 stars in the input population, covering the entire 4k×4k FOV of the WFC3. An analytical model was then used to add approximations to the first-, second-, and third-order ghosts to the F225W image.

Our model quantitatively reproduces the ghost size, position with respect to the source, variation in ghost position as the source is moved on the detector, strength of the ghosts, and the variation in ghost strength with source spectral-energy distribution (Brown & Lupie 2004, ISR WFC3 2004-04). The shape of the ghosts, and the change in shape with source position on the detector, were only reproduced qualitatively; this shape is too complex to reproduce perfectly using analytical functions. However, our simulation is realistic enough to closely resemble the behavior of the actual ghosts and their effects on quantitative stellar photometry. Finally, the images were degraded appropriately for the sky background and the CCD dark current and read noise. Fig. 13 shows the entire simulated 4k×4k GC image in F225W, without filter ghosts.

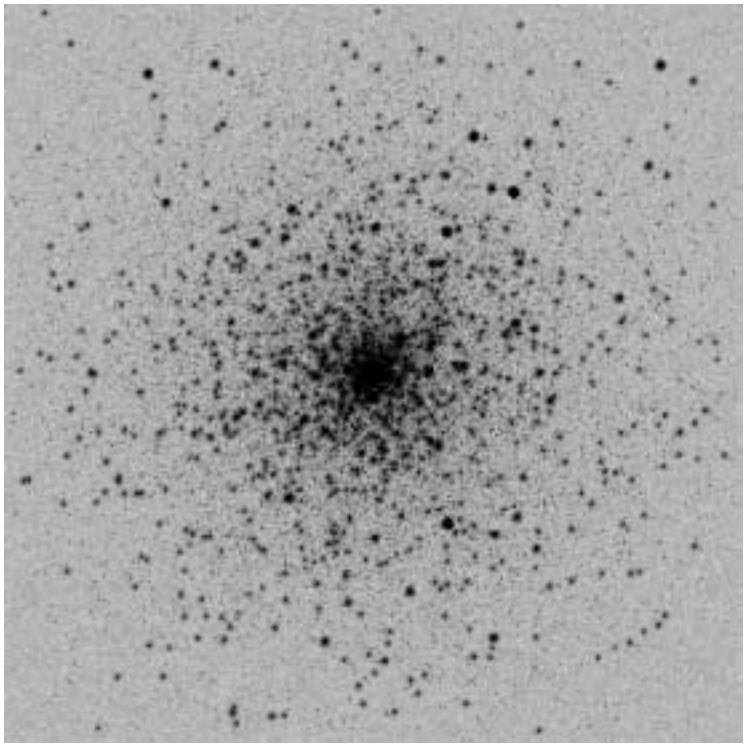

Figure 13: A simulated WFC3 image of a globular cluster in F225W, without filter ghosts. Field of view is 4k×4k pixels, or $156'' \times 156''$. Logarithmic stretch.

Since the ghosts are difficult to see in the entire 4k×4k image, we have zoomed in on small regions in the following figures. Fig. 14 shows a subsection of the simulated F225W image without ghosts, while Fig. 15 shows the same section with the ghosts. In these images, the hot HB stars dominate, and in Fig. 15 their ghosts lie on top of many of the fainter stars (red giants, main-sequence stars, white dwarfs, etc.).

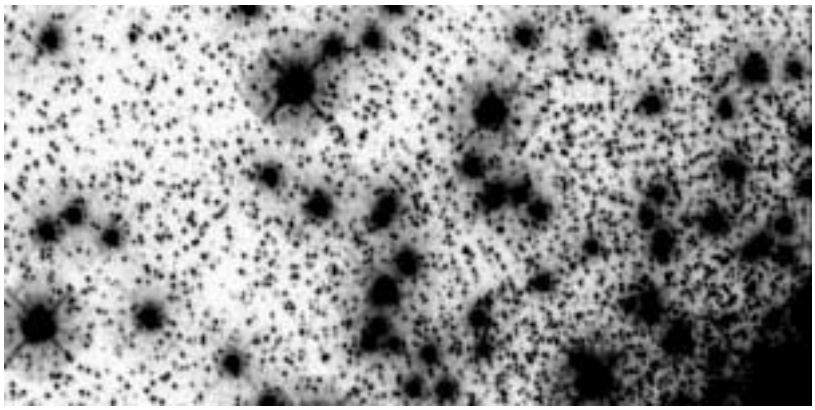

Figure 14: Subsection (512×256 pixels or $20'' \times 10''$) of the simulated WFC3 F225W globular-cluster image, assuming the filter has no ghosts.

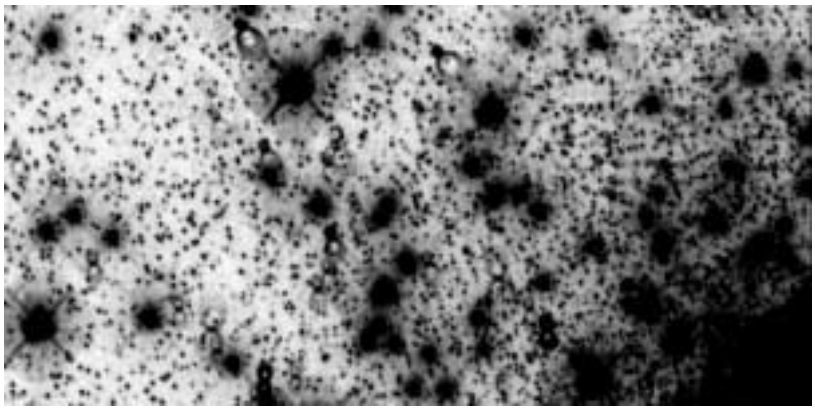

Figure 15: Same subsection of the simulated globular cluster, with simulated F225W ghosts included.

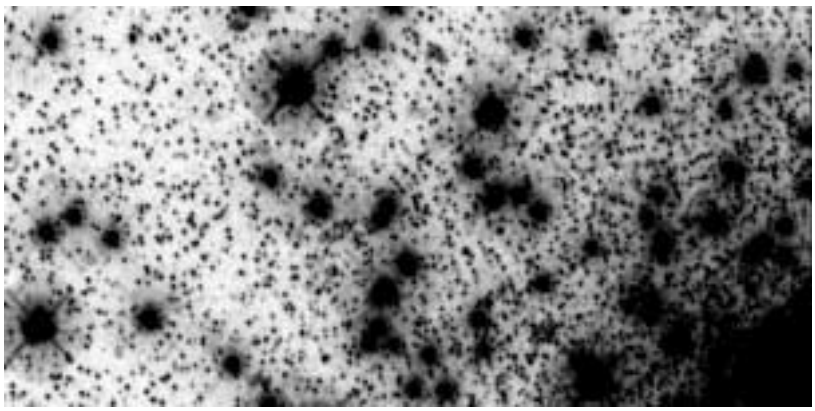

Figure 16: Same subsection as in Figs. 14 and 15, after ghost removal via a two-point dither mitigation. Ghosting is reduced, but artifacts remain and the background has increased significantly relative to the truth image in Fig. 14. The same logarithmic stretch has been used in all three figures.

We now consider the extent to which a dither strategy as described above can mitigate the severe ghosts seen in Fig. 15. To simulate this, we also created two additional images with the same exposure time, but with the first having a dither of (+500,+500) pixels and the second having a dither of (−500, −500) pixels. These images were then registered and combined by rejecting, at each pixel, the brighter value. A more sophisticated adaptive combination algorithm might be employed in the future with actual flight images, which would mask the ghosts only where such masking is needed, thus avoiding a need for twice the observing time to reach a given depth. However, for purposes of this investigation, the resulting combination has an effective exposure time of 5000 sec (given that it is the minimum of two 5000-sec exposures), and so a fair comparison can be made to the other simulated images.

Fig. 16 shows the same image section as in Figs. 14 and 15 above, but with the ghosts partly removed via the two-point dither and pixel-minimum recombination. It is clear that the ghosts have not been removed entirely (because ghosts from two different adjacent bright stars can fall on the same pixel), and moreover the general level of the background has increased significantly. There is no getting around the fact that extended ghosts as severe as those affecting F225W will increase the noise due to the higher background.

We then determined CMDs for the truth image and the dither-mitigated image. There is, of course, a significant impact on the data quality, but, perhaps surprisingly, the impact is not large enough to hamper most of the original science goals.

Fig. 17 shows the baseline CMD recovered from aperture photometry on the original F336W and F225W images, with no simulated ghosts in either image. The object detection was performed in the F336W image only. Note that a "shadow" of the hot HB can be seen toward the bottom of the CMD; this is an artifact caused by false detections of "stars" in the wings of the F336W PSF, and could most likely be removed via PSF-fitting photometry rather than the simple aperture photometry used here.

The F336W object list was then used to identify stars and perform aperture photometry on the ghost-afflicted F225W image of Fig. 15, and the result is shown in Fig. 18. Looking at the faint, redder stars, we see that the scatter has increased significantly, and the detection limit has moved brighter. Thus, for example, measurements of stellar luminosity functions would be affected by loss of sensitivity at the faint end, although it should be possible to estimate the incompleteness factors through artificial-star tests. However, the bright, hot population—which might be the primary aim of imaging at ∼2200 Å—is virtually unaffected.

Using the same F336W object list, aperture photometry was also performed on the F225W image of Fig. 16, in which the ghosts have been mitigated via two-point dithering; the resulting CMD is shown in Fig. 19. Nearly half of the field area was lost in the combined image, but the photometric scatter has been reduced significantly, compared to Fig. 18. The detection limit does not recover to the level seen without ghosts (Fig. 17), but this is expected, due to the increased noise

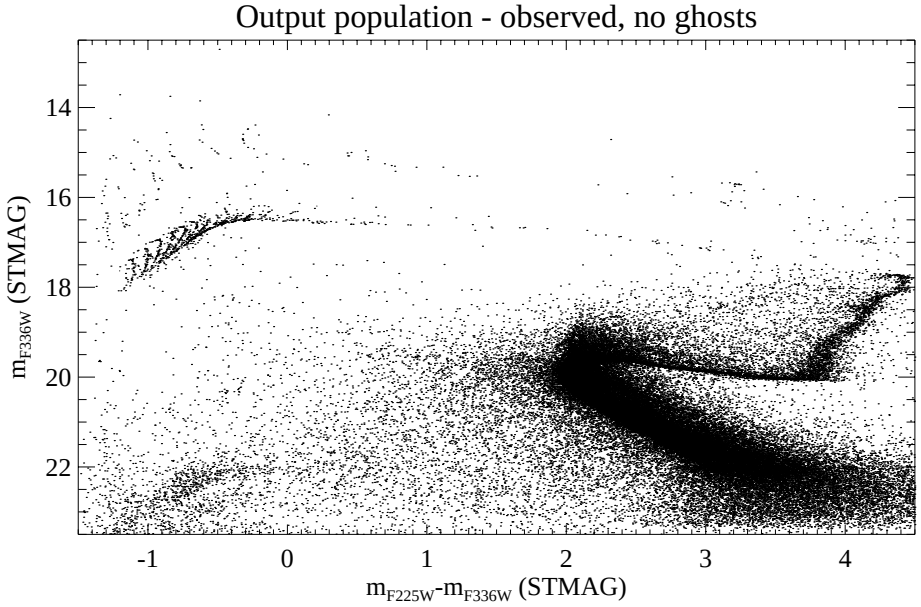

Figure 17: CMD created from object detection on a simulated F336W image and aperture photometry on that image plus a simulated F225W image, assuming the F225W has no ghosts (in reality, the F336W filter has no significant ghosts but the F225W filter does).

in the brighter background of the dithered, ghost-filled images before they were combined.

It is difficult to quantify the loss of accuracy due to the ghosts, since it depends very strongly on the nature of the target field (stellar density, number of bright stars, etc.). However, for this particular simulation, we can take the rms scatter of the $m_{225} - m_{336}$ color as an index. For stars with magnitudes $21 < m_{336} < 22$, the rms is is 0.67 mag when there are no ghosts, 0.76 mag when there are ghosts, and 0.73 mag when the ghosts are mitigated via dithering.

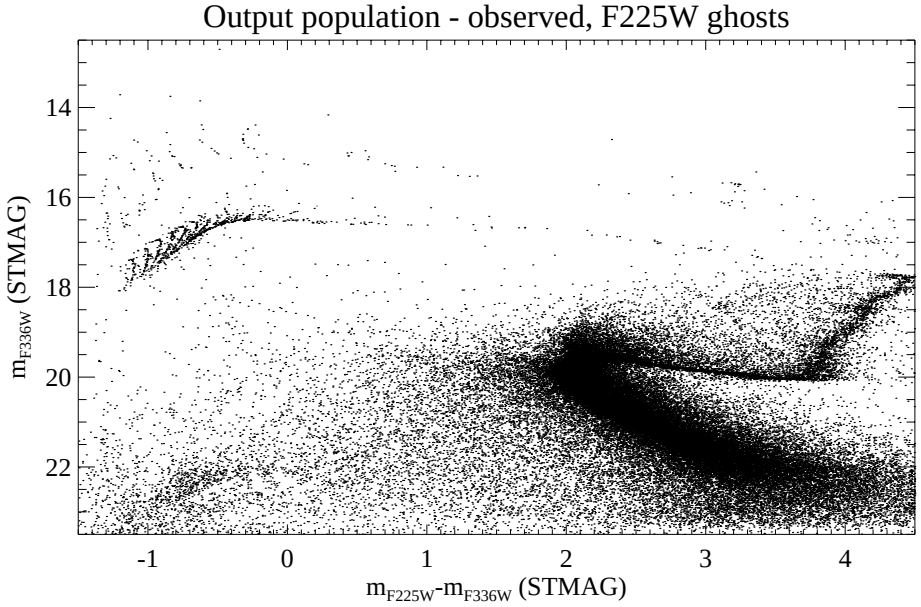

Figure 18: CMD created from object detection on a simulated F336W image and aperture photometry on that image plus a simulated F225W image, assuming the F225W has ghosts. The scatter is higher at the main-sequence turnoff and below, but the hot horizontal branch is virtually unaffected by the ghosts.

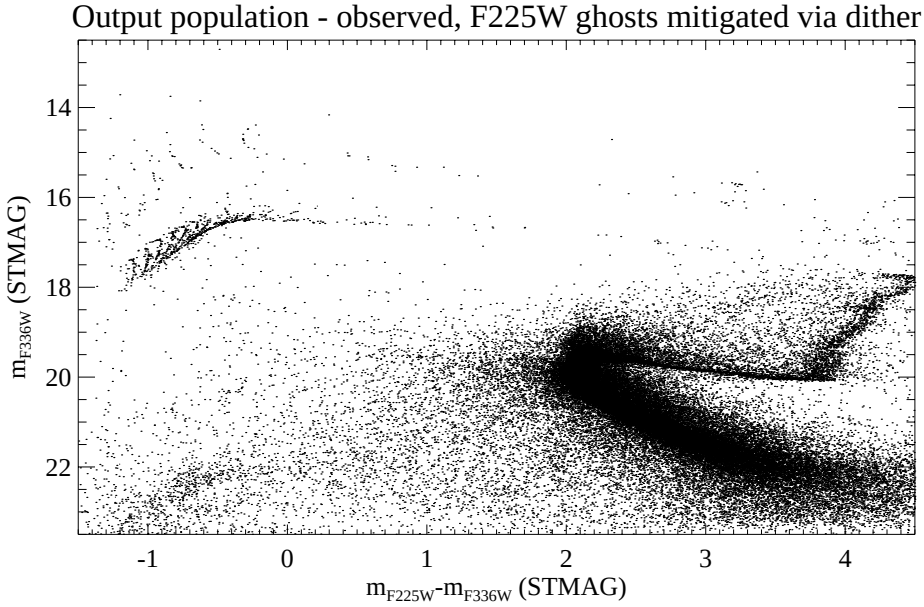

Figure 19: CMD created from object detection on a simulated F336W image and aperture photometry on that image plus a simulated F225W image, assuming the F225W has ghosts but that they have been partially mitigated by combining two dithered images.

F606W Simulations

A similar procedure was used to test the effects of the compact ghosts in the F606W filter. Because the WFC3 throughput using the F606W filter is higher than with F225W, we made another simulation in which the cluster was assumed to be more massive and distant: 500,000 stars lying at 100 kpc, distributed randomly in a Gaussian profile with $\sigma = 500$ pixels. The population was drawn from the Bertelli (1994) isochrones to fainter absolute magnitudes, but there was no extension to a hot HB. Exposures of 1000 sec were simulated in the F438W and F606W filters, using models of the ACS WFC3 PSF in the F555W and F775W filters, respectively, again rotated by 45°. The input population for the simulations is shown in Figs. 20 and 21, with physical and observable parameters, respectively.

Although the F606W filter exhibits at least 13 compact ghosts (see Fig. 5) when examined with monochromatic light, only five of these were detectable in ground test images using a continuum source with a red spectral energy distribution; these are ghosts 1, 2, 3, 5, and 6 in Table 4 of Brown (2004). For the simulations here, these five ghosts were modeled as Gaussians, all somewhat wider than the stellar PSF (with a FWHM ranging from 2.7 to 5.6 WFC3 pixels). Although the strengths of these ghosts are wavelength-dependent, they are very faint (0.01%–0.12% of the source), so our ghost model did not include a dependence on the spectral energy distribution. The positions of these ghosts, relative to the source, vary slightly with the position of the source on the detector, but not nearly as strongly as the variation seen in the extended ghosts of the F225W filter; the ghost positions and the variation in these positions was accurately reproduced by the model. Fig. 22 shows the full 4k×4k simulated GC.

Once again, the ghosts are too subtle to see in the full frame, so Figs. 23 and 24 show a subsection of the F606W image, simulated without filter ghosts and with filter ghosts, respectively.

As before, object detection was done on the filter that does not have ghosts—in this case the F438W image. Aperture photometry was then performed on the F438W image and the ghost-free version of the F606W image. The resulting baseline CMD is shown in Fig. 26. Next, using the same object list, aperture photometry was performed on the F606W image that included ghosts; the result is shown in Fig. 27. Although there is a slight broadening of the faint main-sequence distribution, overall the degradation of the photometry is almost negligible. Of course, this is partly due to the fact that the objects are detected only in the F438W image, which is free of ghosts. In practice, deeper object detection often relies upon a combination of the two bands in a CMD, in which case the compact ghosts might produce false detections in the object list. Some fraction of those would not produce meaningful photometry in the F438W image, and would thus be rejected, but random background fluctuations and superpositions with real stars in the F438W image would allow some of those false detections to persist. Such false detections might be mitigated via PSF-fitting photometry.

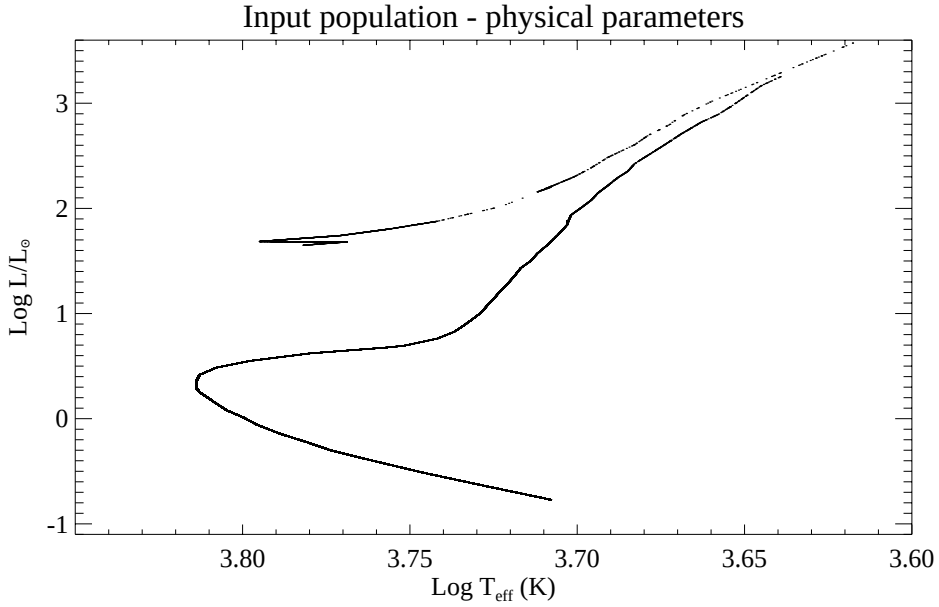

Figure 20: The input population for the F438W and F606W simulated images, shown in terms of physical parameters for the 500,000 stars.

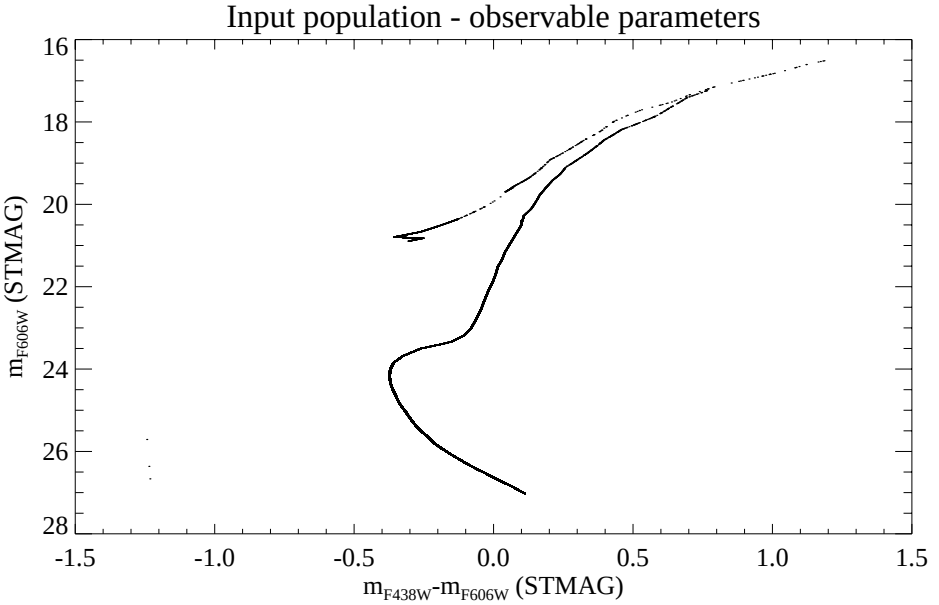

Figure 21: The input population for the F438W and F606W simulated images, shown in terms of observable parameters.

In order to mitigate these faint compact ghosts, one might try, as was done above, dithering or rolling the field. Because the positions of the compact ghosts in F606W (with respect to the source) do not change dramatically with source position on the detector, fairly large dithers would be required to remove the ghosts. To investigate this, we again produced simulated images produced at dithers of (+500,+500)

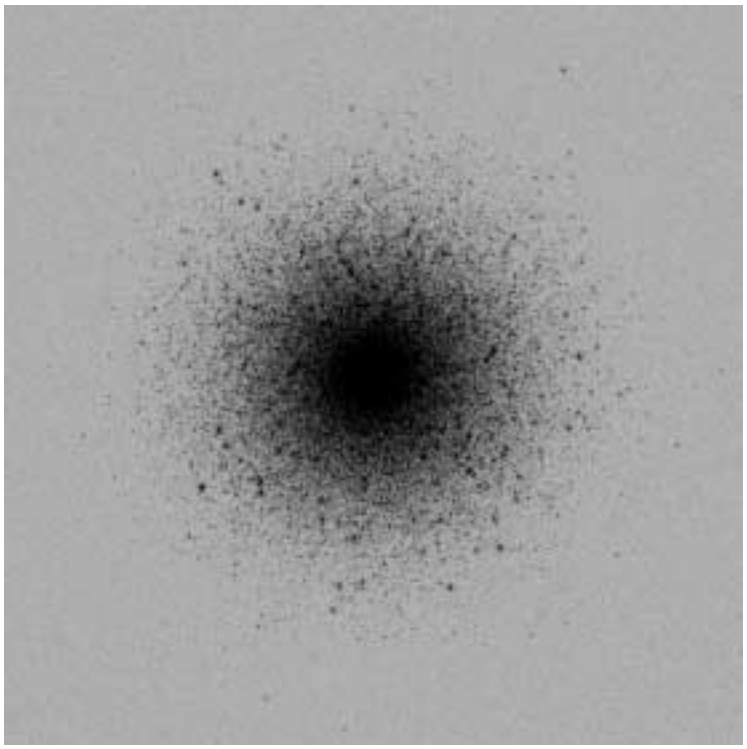

Figure 22: A simulated WFC3 image of a globular cluster in F606W, without filter ghosts. Field of view is 4k×4k pixels, or $156'' \times 156''$. Logarithmic stretch.

pixels and $(-500, -500)$ pixels; these were then combined, as above, once again rejecting at each pixel the brighter value. The resulting cleaned image is shown in Fig. 25. Performing aperture photometry on this image results in a CMD with slightly less scatter (Fig. 28), at the price of losing nearly half of the field area through such dithering. Because the ghosts lie roughly along a diagonal passing through the source, we also simulated an F606W image rolled by 90°. Rotating this image and combining with the unrolled F606W image, again via a minimum, gives the cleaned image shown in Fig. 29, and the CMD shown in Fig. 30. The photometric scatter has been reduced without the loss of field that results from dither mitigation. The PSF has, however, changed significantly: its wings have less structure, and the change in aperture correction has produced an artificial shift in the locus of stars in the CMD (which could be corrected in a more rigorous analysis of the images).

As was the case for the F225W simulations, it is not easy to quantify the effects of the ghosts on F606W photometry, since the effects depend very strongly on the nature of the object being studied. However, we can note that rms scatter in the color for stars with $24 < m_{606} < 25$ only changes by about 1% between the F606W images without and with ghosts, and with ghosts mitigated by dithering. (A meaningful comparison with the roll-mitigated image is not possible because of the significant changes in the simulated PSF.)

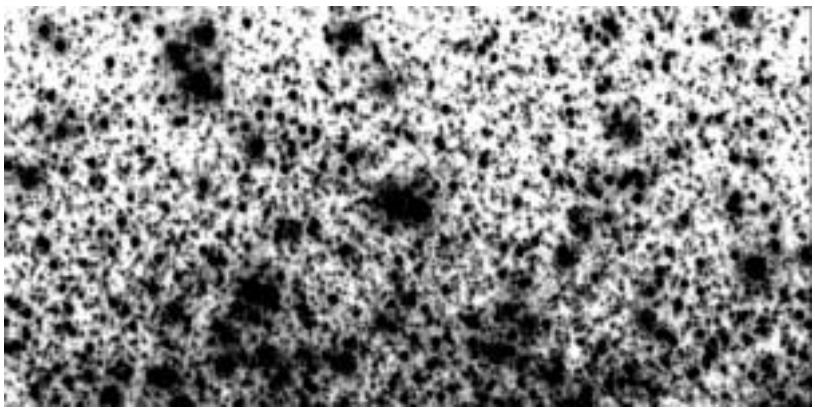

Figure 23: Subsection (512×256 pixels or $20'' \times 10''$) of the simulated WFC3 F606W globular-cluster image, assuming the filter has no ghosts.

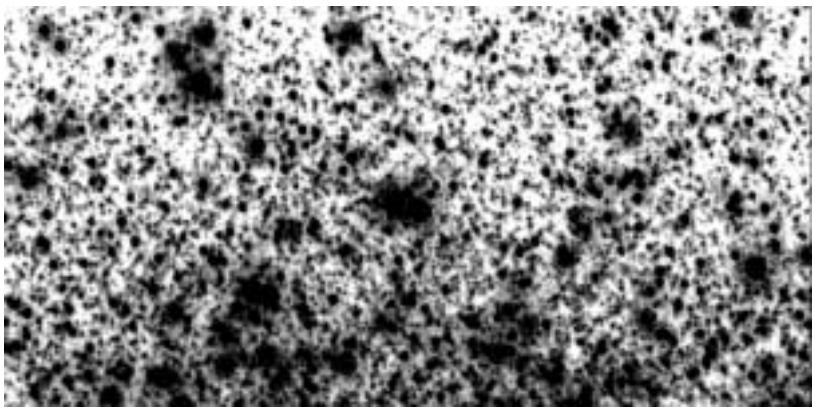

Figure 24: Same subsection, with simulation of F606W ghosts. The ghosts are very subtle, but careful inspection may disclose several of them.

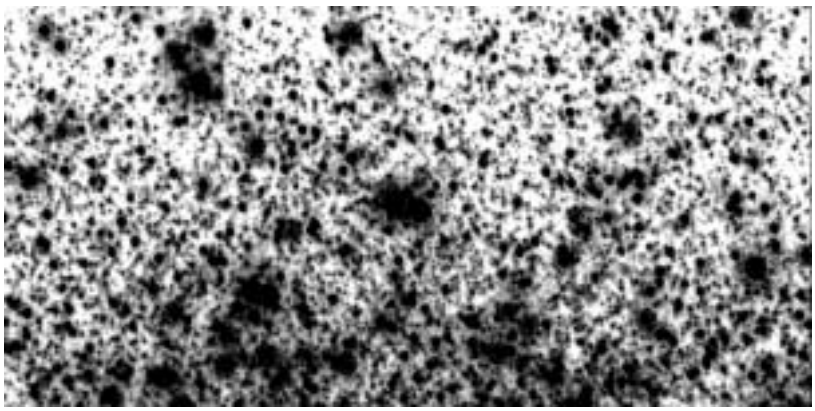

Figure 25: Same subsection, with ghosts that have been mitigated via a two-point dither. The same logarithmic stretch has been used in all three images.

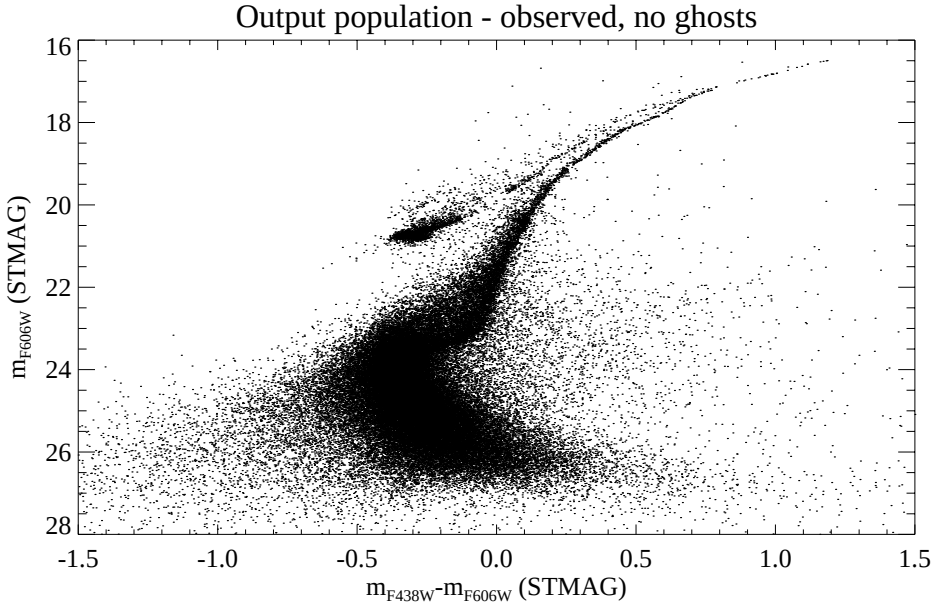

Figure 26: CMD created from object detection on a simulated F438W image and aperture photometry on that image plus a simulated F606W image, assuming the F606W has no ghosts (in reality, the F438W filter has no significant ghosts but the F606W filter does).

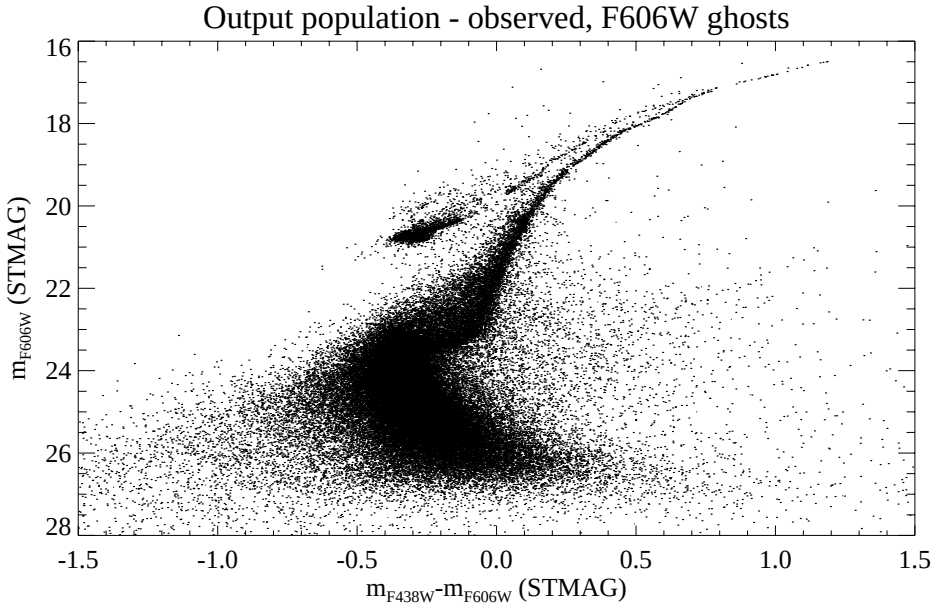

Figure 27: CMD created from object detection on a simulated F438W image and aperture photometry on that image plus a simulated F606W image, assuming the F606W has ghosts. At faint levels there is a modest increase in the scatter.

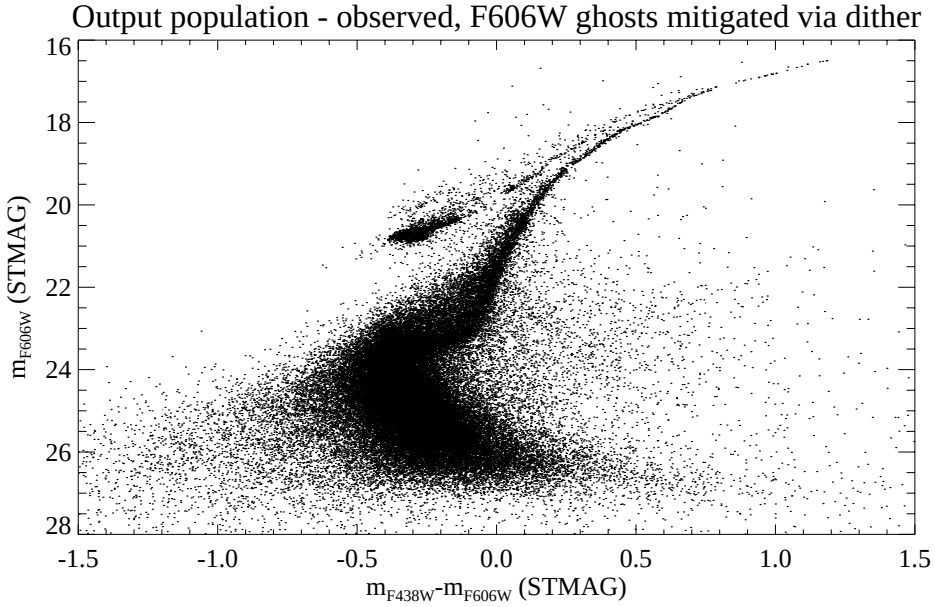

Figure 28: CMD created from object detection on a simulated F438W image and aperture photometry on that image plus a simulated F606W image, assuming the F606W has ghosts but that they have been partially mitigated by combining dithered images.

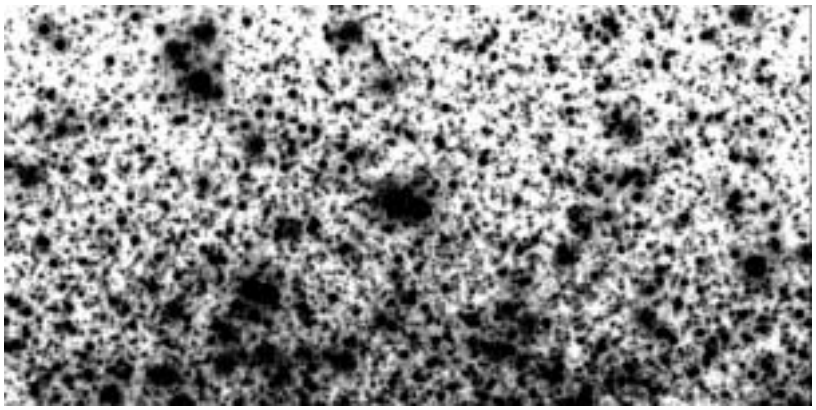

Figure 29: Same subsection of a simulated WFC3 F606W globular cluster image as in Figs. 23-25, with ghosts that have been mitigated via combining two images rotated by 90°.

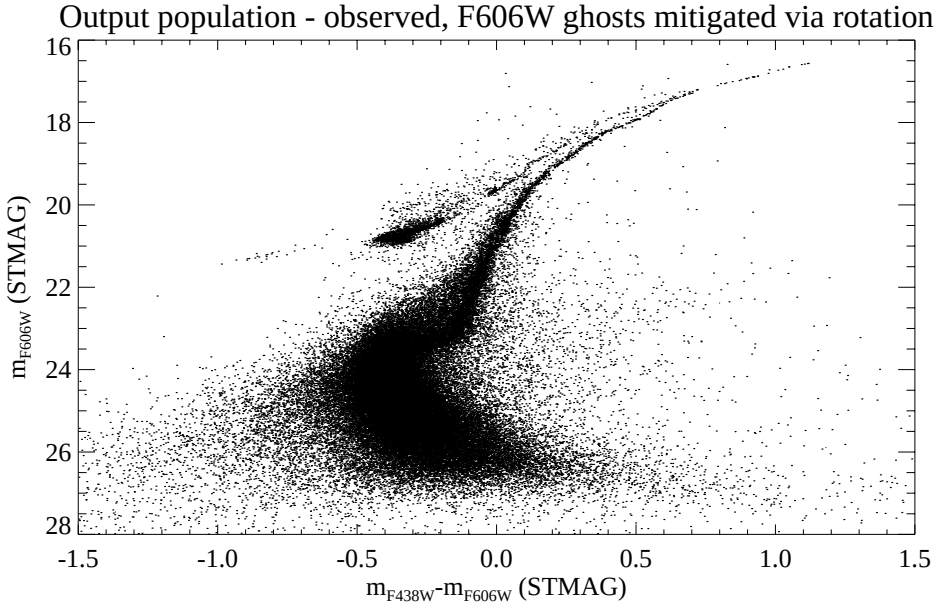

Figure 30: CMD created from object detection on a simulated F4386W image and aperture photometry on that image plus a simulated F606W image, assuming the F606W has ghosts but that they have been partially mitigated by combining images at two different orientations

Conclusions

The above investigation and simulations have led us to the following conclusions:

1. The F225W filter has the most severe ghosting of the WFC3 filter complement. However, the impact of these ghosts on WFC3 science programs varies widely with the nature of the targets to be observed and the scientific goals.

2. For programs involving simple fields covering a small spatial extent, such as studies of the host galaxies of single isolated QSOs, the ghost impact is fairly minimal even in F225W. Morphological classification and some simple measurements are possible even on the ghost-affected images without any mitigation, and straightforward deconvolution routines can remove most of the ghosting in cases where it needs to be removed.

3. However, deconvolution routines do not exist that can deal with extended WFC3 scenes in F225W, because of the strong variation in PSF over the field. For wide-field imaging, it may be possible to mitigate the ghosts successfully though combination of images taken at several different dither positions (at the cost of losing field area), or combining images taken at different spacecraft roll angles (at the cost of additional scheduling complexity and, in some cases, a significant increase in the number of *HST* orbits required to complete the program). However, only fairly simple scenes (containing, for example, only a few widely separated objects) can be fully cleaned of ghosts through such techniques.

4. A complex scene involving widely extended objects, especially one with a wide dynamic range, such as the planetary nebula discussed above, will be irretrievably affected by ghosts as strong as those of F225W. The reason is that a given pixel is overlain by ghosts arising from a wide variety of adjacent bright pixels, and there is no unique method for reassigning the intensities back to the correct source pixels. This remains true even for dithered and rolled images.

5. Thus, individual proposers will have to make a series of complex decisions involving the scientific goals of their programs and the detailed nature of their targets, when developing their observing plans, *and these decisions will have to be made at the time of the Phase I proposal,* since they affect the number of spacecraft orbits needed to accomplish the science.

6. For programs of stellar photometry, the ghosts in F225W appear to have a smaller impact. We showed through our simulations that the main features of color-magnitude diagrams survive the ghost effects with only a fairly minor increase in photometric scatter, especially for stars well above the magnitude limit of the exposures. However, the ghosts create an effect similar to increasing the sky brightness, especially in crowded fields, so for faint photometry it will be necessary to increase the exposure time and/or use dithers or rolls to mitigate the ghosts.

7. The ghosts in the other filters considered in this study (F275W, F606W, F656N) have much lower intensities than those in F225W, and their impact is accordingly much less severe. However, in critical cases (such as extended objects with wide dynamic range), it will be necessary to use dithers or rolls to mitigate these ghosts, so that some programs will require additional spacecraft time to be carried out.

For the most difficult cases (e.g., studies of faint regions immediately adjacent to bright ones), there may be no practical way to fully remove the ghost signatures.

8. Our detailed simulation of the effects of the F606W ghosts on stellar photometry in crowded fields showed that, for most programs, the small gain in accuracy resulting from dithers and/or rolls would not be worth the loss in field area or the additional orbits required.

Recommendations

1. We have shown that the severe ghosts in F225W do compromise some science programs, rather severely in some cases. Mitigation of the ghosts, where possible, may require significant increases in exposure time and orbit allocation, and/or loss of field area. Thus, a more detailed cost-benefit analysis should be performed to assess the merits of replacing this filter vs. flying it as is and accepting these additional costs.

2. Well before the first Phase I proposals are accepted for WFC3 observations involving filters that are affected by ghosts, detailed documentation of their effects and advice for mitigating them should be developed by STScI for use by the astronomical community.

3. The scientific effects of the considerably weaker ghosts in the other filters considered here are significantly less deleterious than those of the strong ones in F225W. In most cases, the penalty in observing efficiency for flying these filters would be fairly modest, although certain especially difficult observations may be compromised. However, again, each proposer would have to make a detailed assessment of the impact on his/her specific program, and STScI should be prepared to provide such advice well in advance of the Phase I proposal deadlines.

4. For any ghost-affected filters that are flown, it will be important to obtain a complete library of PSF images, including dependence on field location and energy distribution of the source. This work should be done initially during ground tests, and on actual stars after launch.